IOP Publishing Measurement Science and Technology
Meas. Sci. Technol. **31** (2020) 045403 (8pp) https://doi.org/10.1088/1361-6501/ab4d2e

Annular-beam dual-detection confocal reflectance microscopy for high-speed three-dimensional surface profiling with an extended volume

Dong-Ryoung Lee[1,2], Dae-Gab Gweon[1] and Hongki Yoo[1]

[1] Department of Mechanical Engineering, Korea Advanced Institute of Science and Technology (KAIST), 291 Daehak-ro, Yuseong-gu, Daejeon 34141, Republic of Korea
[2] Department of Cell Biology, Yale School of Medicine, 333 Cedar street, New Haven, CT 06520, United States of America

E-mail: h.yoo@kaist.ac.kr

Received 27 March 2019, revised 6 September 2019
Accepted for publication 11 October 2019
Published 8 January 2020

Abstract

In this study we propose an annular-beam dual-detection confocal reflectance microscopy (ADDCRM) method for high-speed three-dimensional surface measurements without longitudinal mechanical translation. ADDCRM can measure the axial position of a sample surface using the axial response curve ratio of two photodetectors, each with a different diameter pinhole. Since the height measurement range is limited by the full-width at half-maximum of the ratio curve, an annular beam is used to extend the depth range without reducing the lateral resolution. The experimental results demonstrate that ADDCRM achieves high-speed surface profiling with a doubled-height measuring range compared to conventional Gaussian beams.

Keywords: surface measurement, confocal microscopy, three-dimensional microscopy, height measurement

(Some figures may appear in colour only in the online journal)

1. Introduction

Confocal scanning microscopy (CSM) is a powerful tool for three-dimensional (3D) topography with high resolution due to the capability of point-imaging [1]. CSM requires point illumination and point detection to measure the focal point on the sample plane by rejecting out-of-focus light [2, 3]. With this unique optical structure, CSM can improve its resolution relative to conventional optical microscopy and obtain non-contact and non-destructive optical sectioned images with high signal-to-noise ratio [4, 5]. However, point scanning is necessary for CSM to reconstruct a 3D measurement [6]. In general, the focused laser beam is scanned across the sample in the lateral plane, and this lateral scanning is repeated in the axial direction [7, 8]. The axial scanning of CSM generally moves the objective lens or the sample mechanically. However, mechanical movement generates vibration in the system and repeated lateral scanning is a time consuming process.

To overcome this limitation, researchers have tried to eliminate the repetitive two-dimensional scanning process through approaches such as chromatic confocal microscopy (CCM), differential confocal microscopy (DCM), and divided-aperture differential confocal microscopy (DDCM). CCM, DCM, and DDCM encode the height information so that height can be calculated from the signal without axial scanning [9–24]. First, CCM encodes the height of the sample surface spectrally in the axial direction. Since different wavelengths are focused with different lengths, CCM uses a white light source and a chromatic aberration objective to disperse the light axially depending on the wavelength. We can then measure the height by analyzing the peak wavelength of the spectrum

reflected from the object. However, it is difficult and complex to design an objective and a spectrometer [9–14]. Also, the measurement depth is limited by the chromatic focal shift of the objective lens. DCM, meanwhile, measures the height by using the axial response curve, which relates the measured intensity to the distance from the focal plane. The detector of the DCM consists of two point detectors placed behind and ahead of the focal plane with the same offset. Their axial response curves are axially shifted and their differential curve is used as a lookup table to measure the axial position with a difference of intensities [15–20]. However, the reflectance of the specimen and intensity fluctuation of the laser source affect the differential curve and the accuracy of the height measurement [18]. To measure the axial position accurately, the differential curve divided by one of the two signals is used as a characteristic curve [19] and polychromatic illumination is used [20]. DDCM combines the divided-aperture confocal microscopy and DCM. In other words, it uses the pupil plane of the objective lens, which is divided into illumination and collection to move the airy disc transversely on the detector plane when the object is translated axially, and it measures intensities with two point detectors that have a transverse offset from the optical axis because the linear relationship between the height of the sample surface and the differential signal can be used as a lookup table [21–24].

To achieve accurate and fast 3D volumetric imaging with a simple optical setup, we presented a dual-detection confocal reflectance microscopy (DDCRM) method that uses two different-sized pinholes in front of detectors to obtain different widths of axial response curves and their ratio curve [25–27]. Although each detected signal is proportional to the reflectance of the specimen and the laser power, the intensity ratio removes the proportional factor by dividing each signal. However, since the measurement depth is limited by the half-width of the ratio curve, a wide axial response curve is required to measure the large 3D volume with single lateral scanning during the same measurement time. While the novel methods described above achieve fast 3D imaging, they all suffer from limited imaging depth.

In this paper, we propose using an annular beam to enlarge the measurement range in the axial direction without compromising the lateral resolution, because the annular beam propagates with reduced transverse spreading in comparison with a Gaussian beam [28–30]. We call this technique annular-beam dual-detection confocal reflectance microscopy (ADDCRM), and we demonstrate it by adding a film mask with an annular aperture to the DDCRM. While utilizing the same basic concept of DDCRM as previously presented, ADDCRM is able to encode long depth information. This depth discrimination technique with an extended depth of field can perform large volumes of accurate 3D imaging, independent of the reflectance of the sample surface, with speeds tens to hundreds of times faster than the standard CSM method, which requires volumetric scans.

2. Principles

In confocal microscopy, the point source, the point detector, and the focal point in the object space are in conjugate positions, and there is a pinhole in front of the photo-detector to reject the out-of-focus light, as shown in figure 1(a). While the light is ideally focused on an infinitely small spot, the real focal point is spread by an optical system due to a diffraction-limited aberration. This diffraction pattern of the light at the focal point is called the point spread function (PSF), and the image is formed by the convolution of the object and the PSF. The PSF is given for the objective lens by the following equation [31, 32]:

$$h\left(2u,v\right)=\int_0^1 P\left(\rho\right)\exp\left(-\mathrm{i}u\rho^2\right)J_0\left(v\rho\right)\rho\mathrm{d}\rho, \tag{1}$$

where $P(\rho)$ is the pupil function of the lens, $\rho = r/a$ is the normalized radial coordinates over the lens aperture with radius a, and J_0 is the Bessel function of the first kind of order zero. The pupil function defining the physical size and shape of the lens can be expressed as

$$P\left(\rho\right)=\begin{cases}1, & \varepsilon<\rho<1\\ 0, & \text{otherwise}\end{cases}, \tag{2}$$

where $\varepsilon = r_\varepsilon/a$ is the normalized radius of a central obstruction of radius r_ε.

When the pupil plane is a circular and uniform aperture, the Gaussian beam is focused. Since the Gaussian beam is diffractive, the beam diverges rapidly as it propagates away from the focal point. On the other hand, an annular shaped beam is less diffractive, and thus the depth of focus of the microscope is extended without spreading transversely over distances that exceed the Rayleigh range of a Gaussian beam [33–36]. Figure 1(b) shows the normalized intensity distributions near the focus on the xy and xz planes with $\varepsilon = 0$, 1/3, 1/2, and 2/3. As ε increases, the PSF is elongated in the z direction, but the lateral widths are the same as shown in figure 1(c).

Since a fraction of the PSF is collected by the objective and focused at a corresponding point in the image plane, the intensity varies according to the amount of light that enters the detector. The detected image intensity is thus determined by the PSF properties and the size of the pinhole. The intensity variation curve in the axial direction is called the axial response curve, and it is plotted as a function of the distance from the focal plane of the objective lens [37]. The intensity is highest at the focal plane, and it decreases gradually as the mirror plane moves axially. When we assume a point source and a planar object, the axial response curve in confocal microscopy according to the pinhole size becomes the following [31, 37]:

$$I_{v_\mathrm{p}}\left(R,u\right)=R\int_0^{v_\mathrm{p}}\left|h\left(2u,v\right)\right|^2 v\mathrm{d}v, \tag{3}$$

where R is the reflectance of the sample surface, $h(2u, v)$ is PSF of the objective lens, and the variables u and v are optical

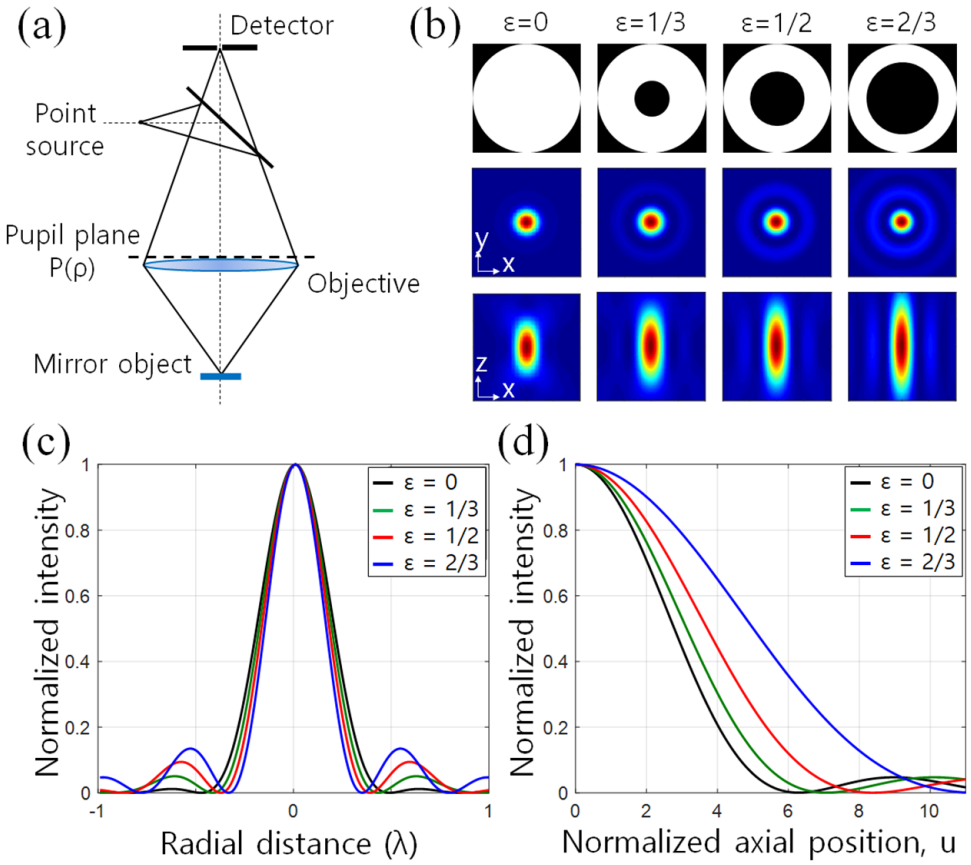

Figure 1. (a) Simplified model of confocal microscopy, (b) intensity distribution at the pupil (top), focal plane (middle), and *xz*-plane (bottom) with $\varepsilon = 0$, 1/3, 1/2, and 2/3, (c) cross-sectional profiles along *x*-axis, and (d) axial response curves.

coordinates in the radial and axial directions, respectively, defined by the following equation:

$$\begin{aligned} v &= \tfrac{2\pi}{\lambda}\, rNA \\ u &= \tfrac{2\pi}{\lambda}\, zNA^2, \end{aligned} \tag{4}$$

where *NA* is the numerical aperture, *r* and *z* are the radial and axial coordinates, respectively, and λ represents the wavelength. v_p in equation (3) represents the radius of the pinhole in the optical coordinate, which determines the width of the axial response curve.

Although the axial response curve indicates the relationship between the axial position of the surface and the measured intensity, the profile of the specimen cannot be rendered with a single axial response curve. This is because the measured intensity is not only related to the axial position but also proportional to the reflectance of the sample and the intensity of the laser. Unlike conventional confocal microscopy, ADDCRM splits the light in the detection path, uses two point detectors with different sized pinholes, and obtains two different widths of the axial response curve, as in DDCRM. The ratio curve above the focal plane indicates a one-to-one relationship between the axial position where the light is reflected on the sample and the intensity ratio measured with two photomultiplier tubes (PMTs), and is independent of the sample and laser conditions. Therefore, ADDCRM is able to encode the lookup table with the intensity ratio curve and reconstruct the accurate 3D sample instantaneously by dividing the intensity values from each detector without axial scanning. When two pinhole diameters of the ADDCRM system are pre-determined, the intensity ratio curve is a function of the axial direction, *z*, and is independent of the constant *R*, as follows [25]:

$$I_R(u) = \frac{R \times I_{v_{p1}}(u)}{R \times I_{v_{p2}}(u)} = \frac{I_{v_{p1}}(u)}{I_{v_{p2}}(u)}, \tag{5}$$

where $I_{v_{p1}}(z)$ and $I_{v_{p2}}(z)$ are the normalized intensities detected by each point detector, respectively.

From equations (1), (3), and (5), the depth range was determined by the half-width of the calibration curve, which is related to the NA of the objective lens, the wavelength, and the size of the pinhole. A low NA of the objective, long wavelength, and large pinholes enlarge the axial range, but degrade the lateral resolution, whereas the pupil function extends the depth of focus without spreading the PSF transversely. The axial response curve of the Gaussian beam decreases rapidly because out-of-focus light is transversely widened and blocked by the pinhole. On the other hand, a needle shaped PSF offers a steady transverse intensity distribution over a large distance along the optical axis, and thus the strength of filtering the out-of-focus light is low. Assuming a point detector, a point source, and a planar object, the axial response curves with various annular beam sizes (ε) are shown in figure 1(d).

In ADDCRM, an annular beam is focused on the sample and detector planes instead of the Gaussian beam to improve

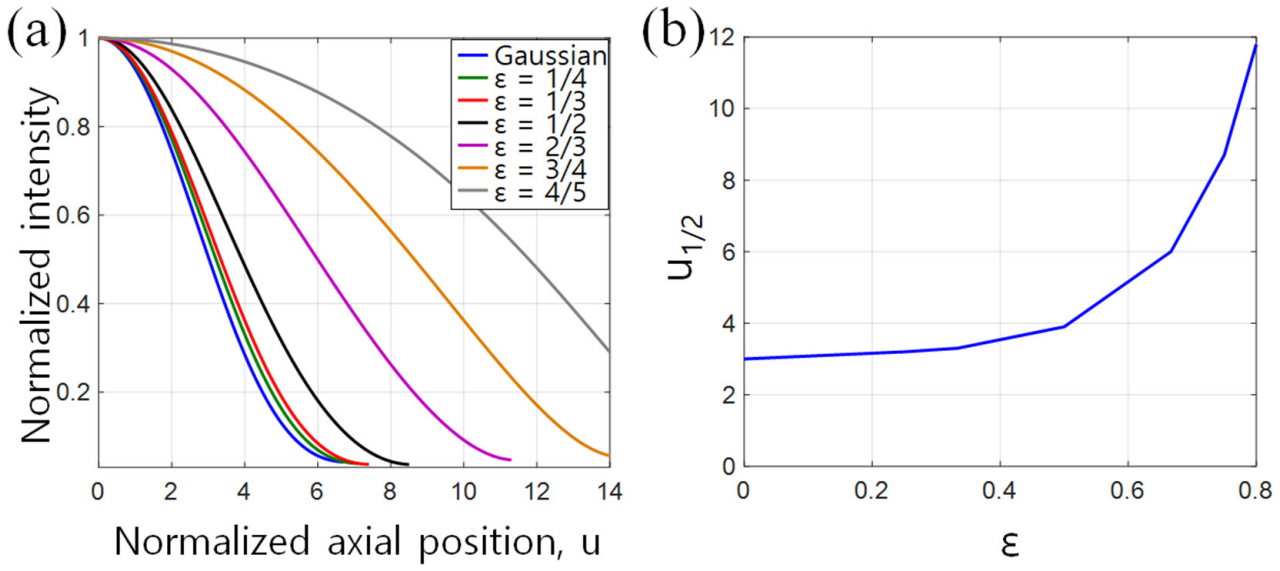

Figure 2. (a) Axial response curves for different normalized inner aperture ε radii. The FWHMs increased as ε increased even when the pinholes were the same size as $v_{p1} = 2.9$ and $v_{p2} = 14.5$. (b) Analysis of the axial response curves. Curve half-widths.

the measurement volume, while maintaining good lateral resolution. In addition, ADDCRM generates two different widths of axial response curves with two different radii of pinholes because different amounts of light pass through the pinholes. We can encode the characteristic curve from two curves of different full-width at half-maximum (FWHM). The characteristic curve indicates a linear relationship between the axial position where light is reflected from the sample and the intensity ratio of two photomultiplier tubes (PMTs). The height of the sample can be measured rapidly by simply analyzing the intensity ratio of the returning light without axial scanning. Figure 2(a) shows the ratio curves of the axial response curves with different annular beam radii when pinhole sizes are predetermined as $v_{p1} = 2.9$ and $v_{p2} = 14.5$, which were determined for DDCRM [25]. As ε increases, the curve width increases. Figure 2(b) shows the half-width of the ADDCRM's calibration curve according to the variation of annular beam size, ε. As ε increases, there is an obvious enhancement in the longitudinal measurement range.

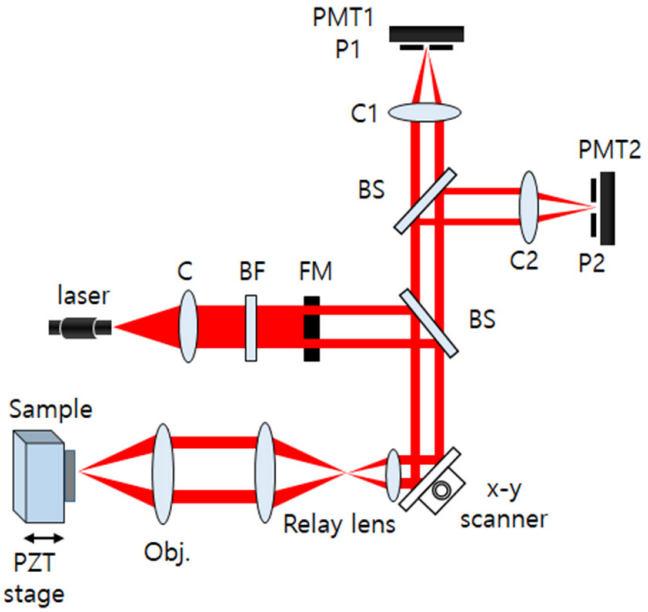

Figure 3. Schematic of the experimental setup. Laser: 488 nm wavelength; C: collimator; BF: band-pass filter; FM: film mask; BS: beam splitter; Obj: objective lens; C1, C2: collecting lenses; P1, P2: pinholes of different sizes.

3. Experimental setup

To verify the performance of the method presented above, an ADDCRM system was built based on the previously demonstrated Gaussian beam DDCRM, as shown in figure 3. The main difference between the ADDCRM and the previous Gaussian beam DDCRM is the film mask (FM) (Core Link, Korea) used to modify a Gaussian beam to an annular beam. The FM was made by drawing a black circle on a transparent PET sheet with a high-resolution laser plotter (50000 DPI (dots per inch)) and customized with a proper diaphragm to shape the laser beam into an annular beam with a normalized radius $\varepsilon = 2/3$. In this experiment, the diameter of the laser beam and the black circle on the film mask were 3 mm and 2 mm, respectively. A laser with a wavelength of 488 nm (35-LAL-030-220, Melles Griot, NY), was collimated by a collimator (HPUCO-23AF-400/700-S-25AC, OZ Optics, Canada), and filtered with a band-pass filter (LL01-488-25, Semrock, NY) with a bandwidth of 1.9 nm. In the ADDCRM system, the center of the circular laser beam is blocked by the FM after being collimated by a collimator (C) and filtered with a band-pass filter (BF). The ring-shaped beam is reflected by a beam splitter (BS010, Thorlabs, NJ) toward the scanning system and scanned transversely. The *x*–*y* scanner is composed of a galvanometer mirror (6240H, Cambridge Technology, MA) and a resonant mirror (000-3015013, GSI Lumonics, MI). A relay lens, which was designed to expand the beam size by a factor of three, allows light to pass onto the back aperture of the objective lens (obj.) (UPLSAPO 4x, Olympus, Japan)

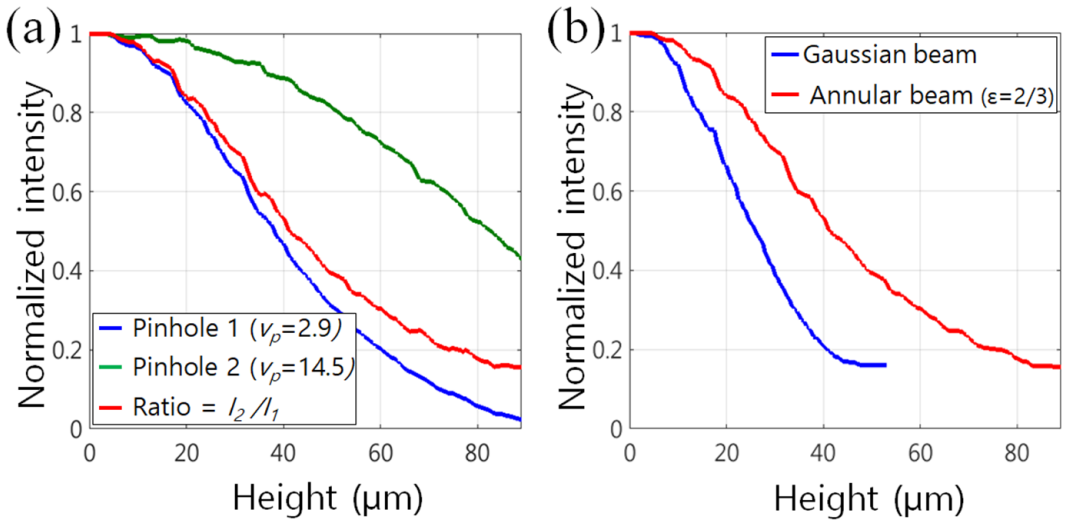

Figure 4. Normalized axial response curves. (a) The curves were obtained using an annular beam. The small pinhole, large pinhole, and ratios are indicated with blue, green, and red lines, respectively. (b) The Gaussian DDCRM ratio curve and ADDCRM ratio curve are indicated with blue and red lines, respectively.

with an effective NA of 0.097 while the beam is scanned. After focusing on the obj. on the sample plane, the beam is reflected, and the reflected light from the object is reversely directed through the obj., relay lens, *x*–*y* scanner, and BS. The beam passes through the BS and is divided by another 50:50 beam splitter into two components that were detected by two PMTs (H6779-20, Hamamatsu, Japan) after being focused by two collecting lenses (NT47-641, Edmund, NJ) onto two pinholes, whose diameters were 30 μm and 150 μm, respectively. To acquire two different axial response curves, two pinhole detectors with different sizes were placed in the focal plane of the detector space.

4. Results and discussion

4.1. ADDCRM axial response test

We measured the axial response curves of the ADDCRM method. A flat mirror was axially scanned over a 95 μm range with 0.5 μm steps by a piezoelectric (PZT) stage (MIPOS, Piezosystem Jena, MA). Two PMTs measured the reflected intensity at each step. Figure 4(a) shows the normalized axial response curves of the ADDCRM method. Two axial response curves having different widths were measured and the ratio of the two intensity curves was thereupon obtained. At the focal plane, the intensities reached their maximum values and decreased continuously as the mirror moved away from the focal plane. Since the axial response curve is symmetrical to the focal plane, only the region above the focal plane was used to avoid ambiguity about the sample located above or below the focal plane. Two kinds of normalized axial response curves were measured by the small and large pinholes, indicated by blue and green lines, respectively, in figure 4(a). The intensity curve decreased rapidly with a small pinhole but decreased slowly with a large pinhole because the strength of filtering the out-of-focus beam degraded as the size of the pinhole increased. The red line shows the ratio of the two intensity

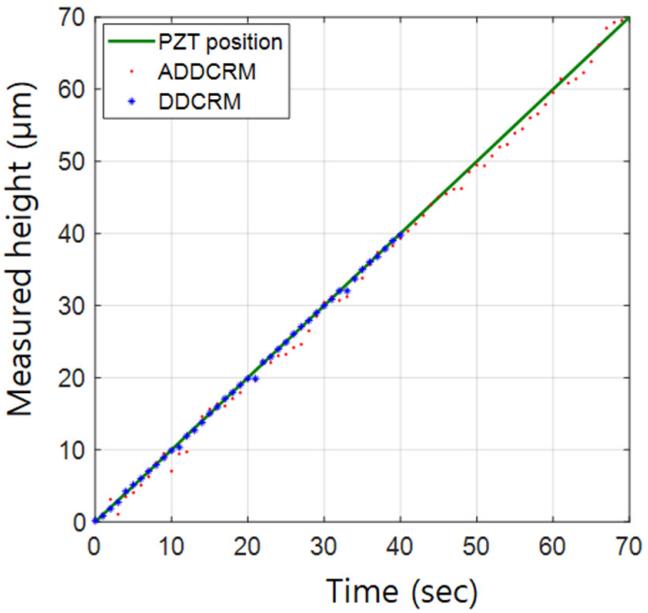

Figure 5. Height variation measurement. The solid green line indicates the PZT input, while the red dots and the blue asterisks indicate mirror heights measured by ADDCRM and DDCRM, respectively.

curves, which calibrates between the intensity ratio of the two PMTs and the axial position of the reflecting surface. When the intensity measured with small pinhole reaches the minimum value, the slope of the ratio curve becomes 0, making it impossible to measure the height. Since the theoretical width of the ratio curve was 88.2 μm, the axial response curves were measured over a 95 μm range. The height calibration curve range was determined over 8.5 μm to 81.5 μm, considering the relatively linear relationship between the intensity ratio and height. Within this range, the calibration curve was fit with a quintic polynomial to generate a height lookup table of the ADDCRM system. The sample height can then be calculated from the intensity ratio without depth scanning by using this

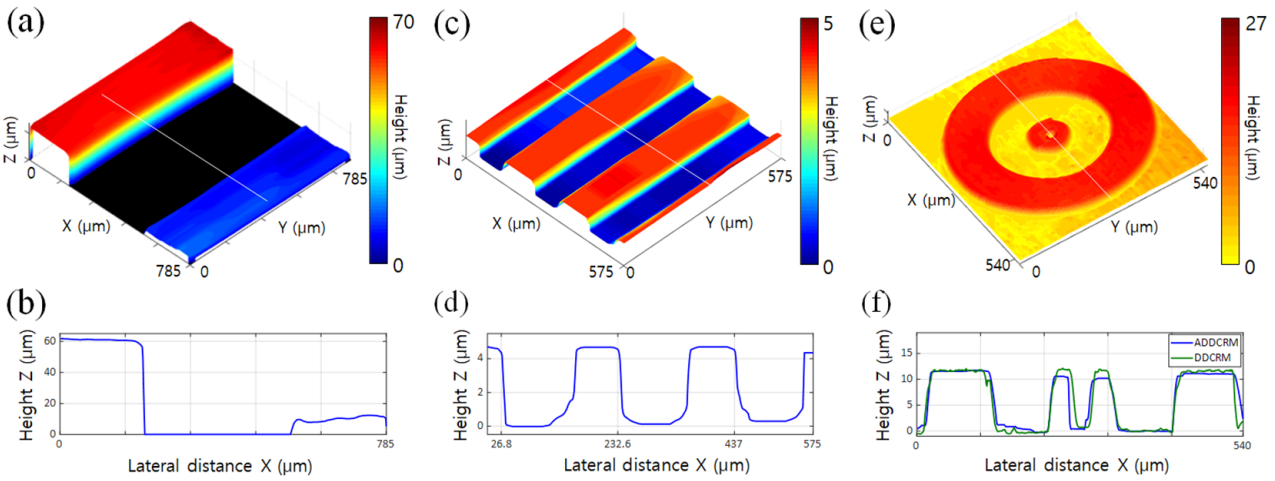

Figure 6. 3D measurement of step-height samples: (a), (c) and (e) 3D profile, and (b), (d) and (f) cross-sectional profiles along the line of the three-step heights.

height lookup table. The standard deviation (SD) between the experimental data and the polynomial curve indicate the accuracy of the axial measurement, and is affected by the slope of the curve and signal-to-noise ratio [38]. In this experiment, the axial measurement range was 73 μm and the SD was 0.68 μm.

The ratio curve of the Gaussian beam was measured by performing the same experimental process with the same ADDCRM setup without using a film mask to compare their widths [25]. The normalized ratio curves were measured with Gaussian and annular beams, which are indicated by blue and red lines, respectively, in figure 4(b). In comparison with the Gaussian beam results, the annular beam almost doubled the FWHM. The measured widths of the curves were verified to be 49.5 μm and 88 μm for Gaussian and annular beams, respectively, which were similar to the theoretical values of 52.8 μm and 88.2 μm, respectively.

To evaluate the performance of the ADDCRM method, the axial movement of the sample was measured, as shown in figure 5. While the flat mirror was continuously elevated by the PZT stage at a rate of 1 μm s^{-1} up to 73 μm, two PMTs detected the intensities at each point, and the height of the reflecting specimen was calculated with the intensity ratio and the lookup table. The solid blue line shows the movement of the PZT stage and the red dots and the blue asterisks indicate the experimental height measured with ADDCRM and DDCRM, respectively, in figure 5. The SD between the height of the stage and the measured value, which evaluated the repeatability of the system, was 0.79 μm.

4.2. 3D imaging

We evaluated the fast 3D imaging performance of ADDCRM, as shown in figure 6. When ADDCRM images a step-height specimen, it can achieve two images that have different intensity profiles simultaneously with a single raster scan and their ratio image. A 3D volume image is then reproduced using the height lookup table and the ratio value of each pixel. Since a high-speed resonant mirror with a scanning rate of 8 kHz and a galvanometer mirror was used as the *x*–*y* scanner, the imaging rate was 15.6 frames s^{-1} with 512 × 512 pixels. Thus, the 3D imaging time was only 64 ms.

Our first test specimen was a master gage (Step master, Mitutoyo, Japan) used for the *z*-axis calibration of optical instruments and the height was certified as 50.11 ± 0.25 μm. Figure 6(a) shows the rendered 3D image of a step-shaped sample in a 785 × 785 μm^2 field of view (FOV) and the cross-sectional profile of the specimen is shown in figure 6(b). For the height, we averaged the height of the flat top and the flat bottom and calcuated the subtraction of the two [39]. The average height of the sample was 51.20 μm and the relative error between the certified value and the height measured by ADDCRM was only 2.18%. When we measured the heights of five different positions on the *y* axis, the SD of the measured value was 1.51 μm. The second sample was a low-profile step height standard (SHS-4.5 QC, VLSI Standards, CA) and the certified step height was reported as 4.422 ± 0.058 μm. Figures 6(c) and (d) show the ADDCRM image of the sample in a FOV of 575 × 575 μm^2 and its cross-sectional profile, respectively. The average height of the sample was measured to be 4.365 μm with the relative error of 1.289% and the SD of 0.12 μm. Finally, we measured a ring-shaped sample (KRISS, Korea), which had been measured by DDCRM in our previous study to compare the lateral resolution between ADDCRM and DDCRM [25]. Figure 6(e) shows the rendered 3D image of the ring-shaped height sample by ADDCRM in a 540 × 540 μm^2 FOV, and figure 6(f) shows the cross-sectional profiles of the specimen as measured with ADDCRM and DDCRM, which are indicated by blue and green lines, respectively. When the height was certified as 11.355 ± 0.086 μm, the average heights of the step measured by ADDCRM and DDCRM were 11.31 μm and 11.38 μm, respectively. The relative error and the SD between the height measured by the confocal microscopy and the ADDCRM are 0.78% and 0.36 μm. To measure the lateral resolution, which is defined as the FWHM of the line spread function, we calculated the edge response function from the edge of the step and differentiated it to derive the line-spread function. In comparison with the DDCRM result, the 3D image of ADDCRM has a steeper edge of the step, and

the lateral resolution of ADDCRM and DDCRM were calculated as 5.15 μm and 6.94 μm, respectively.

5. Conclusion

In this study, we propose a 3D surface profiling technique, called annular-beam dual-detection confocal reflectance microscopy, and we demonstrated ADDCRM by adding a film mask with an annular aperture to the DDCRM. We can also increase its measurement volume by a factor of two with the same imaging speed. ADDCRM enables instantaneous and accurate calculation of the height of a flat surface with the signals, which are simultaneously measured by two-point detectors so that a 3D volumetric image is rendered with single lateral scanning, as in DDCRM. The ADDCRM method extends the range of height measurement in comparison with DDCRM by shaping the laser beam as an annular beam, yet ADDCRM has better lateral resolution than DDCRM. However, ADDCRM is mostly suitable for measuring flat surfaces, similar to DDCRM, because the system is calibrated only for normally reflected light. When the light is scattered by dust or reflected by a curved surface, the height is not accurately calculated with the measured intensity. Further, the maximum measurable tilting angle may be lower than that of conventional laser scanning confocal microscopy. Therefore, as further work, calibrating the tilted optical flat will increase the accuracy by analyzing the deviations from linearity. In addition, the accuracy, defined by the m of the height measurement of the flat surface, was measured to be 0.12 μm, which is large compared to conventional confocal microscopy [40]. However, ultrafast 3D imaging speed is a unique advantage of ADDCRM, which cannot be achieved with conventional confocal microscopy.

In conclusion, ADDCRM was successfully demonstrated by adding a film mask to the DDCRM system. ADDCRM improves the 3D volume size and the lateral resolution in comparison with DDCRM, while 3D imaging speed is dramatically improved compared to conventional confocal microscopy. ADDCRM may be useful for noncontact optical measurement of 3D surface structures for various industrial applications.

Acknowledgments

This research was supported by the Basic Science Research Program through the National Research Foundation of Korea funded by the Ministry of Education (Grant No. NRF-2017R1E1A1A01074822).

ORCID iDs

Hongki Yoo https://orcid.org/0000-0001-9819-3135

References

[1] Hamilton D and Wilson T 1982 Three-dimensional surface measurement using the confocal scanning microscope *Appl. Phys.* B **27** 211–3
[2] Hamilton D, Wilson T and Sheppard C 1981 Experimental observations of the depth-discrimination properties of scanning microscopes *Opt. Lett.* **6** 625–6
[3] Wilson T 2011 Resolution and optical sectioning in the confocal microscope *J. Microsc.* **244** 113–21
[4] Shotton D M 1989 Confocal scanning optical microscopy and its applications for biological specimens *J. Cell Sci.* **94** 175–206
[5] Leeghim H, Ahn M and Kim K 2012 Novel approach to optical profiler with gradient focal point methods *Opt. Express* **20** 23061–73
[6] Wilson T and Sheppard C 1984 *Theory and Practice of Scanning Optical Microscopy* (London: Academic)
[7] Tanaami T, Otsuki S, Tomosada N, Kosugi Y, Shimizu M and Ishida H 2002 High-speed 1 frame ms^{-1} scanning confocal microscope with a microlens and Nipkow disks *Appl. Opt.* **41** 4704–8
[8] Semwogerere D and Weeks E R 2005 *Encyclopedia of Biomaterials and Biomedical Engineering* (London: Taylor and Francis)
[9] Kim T, Kim S H, Do D, Yoo H and Gweon D 2013 Chromatic confocal microscopy with a novel wavelength detection method using transmittance *Opt. Express* **21** 6286–94
[10] Molesini G, Pedrini G, Poggi P and Quercioli F 1984 Focus-wavelength encoded optical profilometer *Opt. Commun.* **49** 229–33
[11] Miks A, Novak J and Novak P 2010 Analysis of method for measuring thickness of plane-parallel plates and lenses using chromatic confocal sensor *Appl. Opt.* **49** 3259–64
[12] Ruprecht A, Wiesendanger T and Tiziani H 2004 Chromatic confocal microscopy with a finite pinhole size *Opt. Lett.* **29** 2130–2
[13] Lin P C, Sun P-C, Zhu L and Fainman Y 1998 Single-shot depth-section imaging through chromatic slit-scan confocal microscopy *Appl. Opt.* **37** 6764–70
[14] Chun B S, Kim K and Gweon D 2009 Three-dimensional surface profile measurement using a beam scanning chromatic confocal microscope *Rev. Sci. Instrum.* **80** 073706
[15] Wang Y, Qiu L, Song Y and Zhao W 2012 Laser differential confocal lens thickness measurement *Meas. Sci. Technol.* **23** 055204
[16] Lee C-H and Wang J 1997 Noninterferometric differential confocal microscopy with 2 nm depth resolution *Opt. Commun.* **135** 233–7
[17] Zou L, Qu J, Hou S and Ding X 2012 Differential confocal technology based on radial birefringent pupil filtering principle *Opt. Commun.* **285** 2022–7
[18] Yang L, Wang G, Wang J and Xu Z 2000 Surface profilometry with a fibre optical confocal scanning microscope *Meas. Sci. Technol.* **11** 1786
[19] Qiu L, Liu D, Zhao W, Cui H and Sheng Z 2014 Real-time laser differential confocal microscopy without sample reflectivity effects *Opt. Express* **22** 21626–40
[20] Tan J, Liu J and Wang Y 2010 Differential confocal microscopy with a wide measuring range based on polychromatic illumination *Meas. Sci. Technol.* **21** 054013
[21] Wang Y, Qiu L, Zhao X and Zhao W 2017 Divided-aperture differential confocal fast-imaging microscopy *Meas. Sci. Technol.* **28** 035401
[22] Zhao W, Liu C and Qiu L 2012 Laser divided-aperture differential confocal sensing technology with improved axial resolution *Opt. Express* **20** 25979–89
[23] Qiu L, Wang Y, Wu H, Sun Y, Cui H, Zhao W, Yuan L and Zhan C 2018 Three-dimensional resolution-enhancement divided aperture correlation-differential confocal microscopy with nanometer axial focusing capability *Opt. Express* **26** 2314–24

[24] Shao R, Zhao W, Qiu L, Wang Y, Wu H and Zhang R 2019 Divided-aperture subtraction-differential confocal method with nanoscale axial resolution *Appl. Opt.* **58** 3252–9
[25] Lee D-R, Kim Y-D, Gweon D-G and Yoo H 2014 High speed 3D surface profile without axial scanning: dual-detection confocal reflectance microscopy *Meas. Sci. Technol.* **25** 125403
[26] Lee D-R, Kim Y-D, Gweon D-G and Yoo H 2013 Dual-detection confocal fluorescence microscopy: fluorescence axial imaging without axial scanning *Opt. Express* **21** 17839–48
[27] Lee D, Gweon D G and Yoo H 2018 Multipoint scanning dual-detection confocal microscopy for fast 3D volumetric measurement *J. Microsc.* **270** 200–9
[28] Zhao W, Tan J and Qiu L 2004 Bipolar absolute differential confocal approach to higher spatial resolution *Opt. Express* **12** 5013–21
[29] Thériault G, De Koninck Y and McCarthy N 2013 Extended depth of field microscopy for rapid volumetric two-photon imaging *Opt. Express* **21** 10095–104
[30] Planchon T A, Gao L, Milkie D E, Davidson M W, Galbraith J A, Galbraith C G and Betzig E 2011 Rapid three-dimensional isotropic imaging of living cells using Bessel beam plane illumination *Nat. Methods* **8** 417–23
[31] Gu M 1996 *Principles of Three-Dimensional Imaging in Confocal Microscopes* (Singapore: World Scientific)
[32] Gu M 1995 Three-dimensional space-invariant point-spread function for a single lens *J. Opt. Soc. Am.* A **12** 1602–4
[33] Lin Y, Seka W, Eberly J, Huang H and Brown D 1992 Experimental investigation of Bessel beam characteristics *Appl. Opt.* **31** 2708–13
[34] Indebetouw G 1989 Nondiffracting optical fields: some remarks on their analysis and synthesis *J. Opt. Soc. Am.* A **6** 150–2
[35] McLeod J H 1954 The axicon: a new type of optical element *J. Opt. Soc. Am.* **44** 592
[36] Durnin J, Miceli J and Eberly J H 1988 Comparison of Bessel and Gaussian beams *Opt. Lett.* **13** 79–80
[37] Wilson T and Carlini A 1987 Size of the detector in confocal imaging systems *Opt. Lett.* **12** 227–9
[38] Cha S, Lin P C, Zhu L, Sun P-C and Fainman Y 2000 Nontranslational three-dimensional profilometry by chromatic confocal microscopy with dynamically configurable micromirror scanning *Appl. Opt.* **39** 2605–13
[39] Moschetti G, Forbes A, Leach R K, Jiang X and O'Connor D 2016 Phase and fringe order determination in wavelength scanning interferometry *Opt. Express* **24** 8997–9012
[40] Yoo H-K, Lee S-W, Kang D-K, Kim T-J, Gweon D-G, Lee S-W and Kim K-S 2006 Confocal scanning microscopy: a high-resolution nondestructive surface profiler *Int. J. Precis. Eng. Manuf.* **7** 3–7